Improved quantitative ^{90}Y bremsstrahlung SPECT/CT reconstruction with Monte Carlo scatter modeling

Yuni K. Dewaraja[a)]
Department of Radiology, University of Michigan Medical School, Ann Arbor, MI, USA

Se Young Chun
School of Electrical and Computer Engineering, Ulsan National Institute of Science and Technology, Ulsan, Korea

Ravi N. Srinivasa and Ravi K. Kaza
Department of Radiology, University of Michigan Medical School, Ann Arbor, MI, USA

Kyle C. Cuneo
Department of Radiation Oncology, University of Michigan Medical School, Ann Arbor, MI, USA

Bill S. Majdalany
Department of Radiology, University of Michigan Medical School, Ann Arbor, MI, USA

Paula M. Novelli
Department of Radiology, University of Pittsburgh, Pittsburgh, PA, USA

Michael Ljungberg
Department of Medical Radiation Physics, Lund University, Lund, Sweden

Jeffrey A. Fessler
Department of Electrical Engineering and Computer Science, University of Michigan, Ann Arbor, MI, USA

Purpose: In ^{90}Y microsphere radioembolization (RE), accurate post-therapy imaging-based dosimetry is important for establishing absorbed dose versus outcome relationships for developing future treatment planning strategies. Additionally, accurately assessing microsphere distributions is important because of concerns for unexpected activity deposition outside the liver. Quantitative ^{90}Y imaging by either SPECT or PET is challenging. In ^{90}Y SPECT model based methods are necessary for scatter correction because energy window-based methods are not feasible with the continuous bremsstrahlung energy spectrum. The objective of this work was to implement and evaluate a scatter estimation method for accurate ^{90}Y bremsstrahlung SPECT/CT imaging.

Methods: Since a fully Monte Carlo (MC) approach to ^{90}Y SPECT reconstruction is computationally very demanding, in the present study the scatter estimate generated by a MC simulator was combined with an analytical projector in the 3D OS-EM reconstruction model. A single window (105 to 195-keV) was used for both the acquisition and the projector modeling. A liver/lung torso phantom with intrahepatic lesions and low-uptake extrahepatic objects was imaged to evaluate SPECT/CT reconstruction without and with scatter correction. Clinical application was demonstrated by applying the reconstruction approach to five patients treated with RE to determine lesion and normal liver activity concentrations using a (liver) relative calibration.

Results: There was convergence of the scatter estimate after just two updates, greatly reducing computational requirements. In the phantom study, compared with reconstruction without scatter correction, with MC scatter modeling there was substantial improvement in activity recovery in intrahepatic lesions (from > 55% to > 86%), normal liver (from 113% to 104%), and lungs (from 227% to 104%) with only a small degradation in noise (13% vs. 17%). Similarly, with scatter modeling contrast improved substantially both visually and in terms of a detectability index, which was especially relevant for the low uptake extrahepatic objects. The trends observed for the phantom were also seen in the patient studies where lesion activity concentrations and lesion-to-liver concentration ratios were lower for SPECT without scatter correction compared with reconstruction with just two MC scatter updates: in eleven lesions the mean uptake was 4.9 vs. 7.1 MBq/mL ($P = 0.0547$), the mean normal liver uptake was 1.6 vs. 1.5 MBq/mL ($P = 0.056$) and the mean lesion-to-liver uptake ratio was 2.7 vs. 4.3 ($P = 0.0402$) for reconstruction without and with scatter correction respectively.

Conclusions: Quantitative accuracy of ^{90}Y bremsstrahlung imaging can be substantially improved with MC scatter modeling without significant degradation in image noise or intensive computational requirements. © *2017 American Association of Physicists in Medicine* [https://doi.org/10.1002/mp.12597]

Key words: ^{90}Y, bremsstrahlung, radioembolization, reconstruction, SPECT/CT

1. INTRODUCTION

Internal emitter therapy with ^{90}Y is associated with promising clinical results in radioembolization (RE) for liver malignancies[1] and radioimmunotherapy (RIT) for non-Hodgkin's lymphoma (NHL).[2] In addition, there are several ongoing clinical trials for ^{90}Y labeled agents including ^{90}Y DOTA-TOC peptide receptor radionuclide therapy for neuroendocrine tumors and ^{90}Y-clivatuzumab tetraxetan RIT for pancreatic cancer.[3] These novel therapeutic applications have sparked growing interest in quantitative imaging of ^{90}Y,[4–8] an almost pure beta emitter (average energy, 0.94 MeV; maximum energy, 2.3 MeV; mean tissue penetration, 2.5 mm; half-life, 64 h).[9] In RE, accurate post-therapy activity quantification is important for establishing lesion absorbed dose vs. response and normal liver absorbed dose vs. toxicity relationships for future treatment planning. In addition, accurate assessment of the post-therapy microsphere distribution is important for safety because of the potential for unexpected deposition outside the liver.

The lack of gamma photons simplifies radioprotection of nontarget organs and other personnel, but complicates quantitative imaging of ^{90}Y; it involves SPECT via bremsstrahlung photons produced by the betas[4] or PET via a very low abundance positron in the presence of bremsstrahlung.[7] PET has the advantage of superior resolution that can lead to better quantification of smaller lesions, but a disadvantage is the high noise associated with low (true) count-rates in the presence of high random fractions.[10] In addition, the fact that SPECT imaging is more widely accessible and cost effective than PET makes it a viable contender for quantitative ^{90}Y imaging. However, standard SPECT reconstruction algorithms available in the clinic are designed for gamma-rays with well-defined energies and not for bremsstrahlung photons that have a continuous energy spectrum. Those reconstruction methods are suboptimal for ^{90}Y primarily because of penetration/downscatter from photons extending to 2.3 MeV, and the infeasibility of using window-based scatter correction with a continuous spectrum. In addition, less than 3% of ^{90}Y beta interactions in tissue yield bremsstrahlung photons > 50-keV,[11,12] so low count-rates are encountered when imaging under low uptake conditions. To overcome some of these limitations Rong et al.[5] and Elschot et al.[6] developed specialized ^{90}Y SPECT reconstruction methods. For modeling scatter effects Rong et al. used a precalculated scatter kernel approach while Elschot et al. used a fast fully MC forward projector for 'on the fly' estimation. MC scatter estimation is generally accepted to be more accurate for regions with heterogeneous attenuation and for multiorder scatter than the scatter kernel approach. However, a fully MC approach to ^{90}Y SPECT reconstruction is computationally very demanding. Furthermore, a fully MC forward projector would be prohibitively large to store as a matrix for 3D reconstruction[13] so one must use an unmatched back-projector, causing convergence issues with some iterative algorithms.

Hence, in the present study we use the approach of using MC to generate only the scatter estimate. Following,[14] during each iteration we add this scatter estimate to the forward projection of the current activity estimate formed using an analytical projector based on a system matrix that accounts for attenuation and collimator response. Previously, our group demonstrated this approach in ^{131}I SPECT, where initial iterations used a triple energy window scatter correction, and later iterations used MC-based scatter estimates.[15] Moore et al. used a similar approach for ^{111}In SPECT.[16] Correcting bremsstrahlung SPECT is more challenging because the scatter contribution is substantially higher and because window-based correction is infeasible even for the initial iterations. Because the scatter estimate may not need to be updated at each iteration, as we demonstrated for ^{131}I,[15] minimizing MC computation time is less critical with our approach using an analytical projector than with a fully MC projector. Thus, our MC simulations model detailed photon transport in the object and camera, including the collimator, avoiding approximations. In addition, because the MC estimated scatter is not part of the system matrix, we use a back-projector that is the exact transpose of the system matrix, thereby avoiding the 'mismatch' that is present in methods that include scatter in the forward projector matrix but not in the backprojector due to the demands on memory and computation.[17]

Multiwindow modeling approach to bremsstrahlung reconstruction use a wider acquisition window while maintaining an accurate measurement model. Multiwindow modeling was combined with a single wide acquisition window in the work of Rong et al. (100–500-keV)[5] and Elschot et al. (50–250-keV)[6] while we investigated combining multiwindow acquisition with multiwindow reconstruction for two energy ranges (105–285-keV and 100–700-keV).[18] While a wider range of the bremsstrahlung energy spectrum is necessary for low count-rate applications, such as imaging following ^{90}Y RIT, a single-window approach with a narrower energy range is sufficient for imaging following RE where there is high focal uptake in the liver. This is particularly true in RE with glass microspheres, where typically 2–4 GBq are infused to the liver. Thus, in the present study, we use a single, relatively narrow acquisition/reconstruction window (105 to 195-keV) that allows the use of a single-energy attenuation map, scatter map and collimator detector response (CDR) function.

This paper compares the proposed single-window ^{90}Y SPECT reconstruction using MC scatter estimation with reconstruction without scatter correction both qualitatively and quantitatively using metrics such as activity recovery, noise and visibility in a phantom study. Finally to demonstrate clinical applicability, our reconstruction approach is applied to five postradioembolization SPECT/CT patient studies to determine lesion activity concentrations and lesion-to-liver uptake ratios.

2. METHOD

2.A. Measurement model

We used a single relatively narrow energy window for both the acquisition and for the projector modeling with the following statistical model:

$$Y_i \sim \text{Poisson}\left\{ \left(\sum_{j=1}^{J} a_{ij} x_j \right) + s_i \right\}, \tag{1}$$

where Y_i denotes the number of counts measured in the ith detector pixel, a_{ij} denotes elements of the system matrix A that models effects of depth-dependent attenuation and collimator/detector blur for a photon leaving the jth voxel toward the ith detector pixel, s_i denotes the scatter 'contamination' component for the ith detector pixel and $x = (x_1, \ldots, x_J)$ denotes the vector of unknown ^{90}Y activity voxel values. We use a fast rotate-attenuate-convolve-sum approach to compute the forward projection multiplication Ax[19] at each iteration, to which we add the scatter estimate in the denominator of the expectation-maximization (EM) algorithm.[14]

The above model combines a system matrix A with scatter s_i estimated by MC. This approach allows us to use an exact matrix transpose A^T as the back-projector that considers only attenuation and detector blur (not scatter), matching the forward projector. In our formulation, the first term of Eq. (1) consists of full-energy (primary) events, which are defined as events that originate with a bremsstrahlung photon energy within the energy range of the acquisition window and deposit their total energy in the detector crystal (Table I). The second term consists of scatter contamination events (estimated by MC), including scatter events that originate with emission energies within the acquisition window as well as downscatter events that originate with emission energies outside the window (Table I).

2.A.1. SIMIND scatter estimate

We use the SIMIND MC code[20] to estimate the scatter contamination component s_i in Eq. (1). The input to SIMIND is the current reconstruction of the ^{90}Y distribution, which describes the beta decay spatial distribution. As described previously,[4,5] because SIMIND does not include electron transport, a precalculated spectrum of bremsstrahlung photons[12,21] is used to sample the photon emission energy and a

TABLE I. Full-energy events and scatter estimate that make up the first and second terms of the measurement model [Eq. (1)]. Attenuation in the object and CDR are included in either the system matrix or the scatter estimate according to the rightmost column.

Emission (keV)	Object scatter?	Interaction in collimator	Last interaction in crystal	Modeled in system matrix or MC scatter estimate?
< 105[a]	Excluded			
105–195	Yes	Any	Any	Scatter estimate[b]
	No	Scatter[c]	Any	Scatter estimate[b]
	No	Geometric or penetration	Scatter	Scatter estimate[b]
	No	Geometric or penetration	Photoabsorption[d]	System matrix (full energy event[e])
> 195	Yes	Any	Any	Scatter estimate (downscatter)[b]
	No	Scatter	Any	Scatter estimate (downscatter)[b]
	No	Geometric or penetration	Scatter	Scatter estimate (downscatter)[b]
	No	Geometric or penetration	Photoabsorption[d]	Excluded (full energy deposited in crystal, but > 195-keV)

[a]Photon cutoff energy in SIMIND was set at 90-keV to allow for energy resolution effects.
[b]Ignored if detected energy is outside 105–195-keV.
[c]Scatter in camera components such as the backscatter layer is treated in the same manner.
[d]Includes scatter in crystal followed by photoabsorption.
[e]Detected energy = bremsstrahlung emission energy.

distance histogram is used to account for the distance between the beta decay and bremsstrahlung generation.[5] Then, detailed photon transport physics in the object and camera is included with explicit modeling of penetration and scatter in the collimator. Because explicit modeling of all the structures behind the crystal is not feasible, a 5-cm glass 'backscatter layer' was used in the model.[22]

2.A.2. Detector response model

For the system matrix A, we computed the detector response for primary photons only including effects of the collimator response, penetration, and crystal scatter. Here, we simulated (SIMIND) a point-like source in air at six distances to the collimator (2, 5, 10, 15, 20, 25-cm) with a photon emission energy corresponding to the central energy of the acquisition window. To account for the beta range effects (finite distance between location of decay and bremsstrahlung emission), we took the approach of Elschot et al.[6] and sampled the photon emission position from within a small sphere instead of a point. Using a high-energy (HE) collimator with a relatively low energy acquisition window (105 to 195-keV), the CDR was well-fitted by a Gaussian function, and did not require modeling the penetration tails that are prominent when using higher energy acquisition windows.[23]
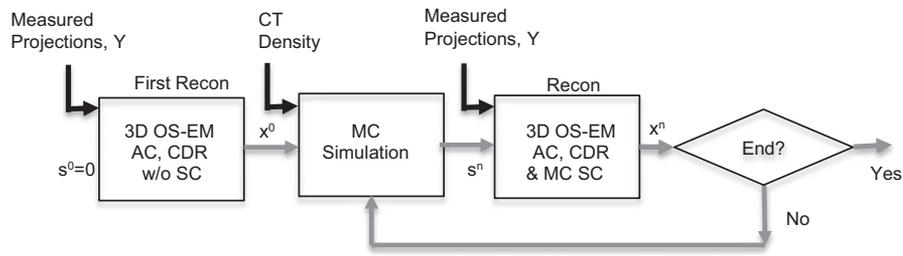
FIG. 1. Flowchart illustrating combination of Monte Carlo scatter estimation with an analytical forward projector.

2.B. Image reconstruction with MC scatter

Our OS-EM algorithm,[24] developed for conventional SPECT reconstruction, was used here with the above described scatter estimation and CDR model. Initial iterations were performed without scatter ($s^0 = 0$ in Fig. 1) but with both attenuation and CDR modeling corresponding to the center energy of the acquisition window. This initial reconstruction yields an activity map estimate and together with the CT-based density map defines the input for SIMIND to generate the first scatter estimate. With appropriate scaling (see below), we used this MC scatter estimate in the next several iterations of OS-EM. This process was repeated with subsequent updates of the SIMIND scatter estimate.

To scale the scatter estimate appropriately, we conjecture that the unknown scatter component s_i is proportional to the SIMIND scatter counts s_i^{SIMIND} and the measured counts Y_i are also proportional to the total SIMIND generated counts Y_i^{SIMIND} with the same fraction at each pixel i as follows:

$$s_i = \alpha_i s_i^{SIMIND}, \ Y_i = \alpha_i Y_i^{SIMIND} \tag{2}$$

The SIMIND MC simulator generates the estimates $Y_i^{SIMIND}, s_i^{SIMIND}$ using as input the estimated image from the previous iteration. The fraction α_i is:

$$\alpha_i = \frac{Y_i}{Y_i^{SIMIND}} \tag{3}$$

The scatter estimate for subsequent iterations is:

$$s_i = s_i^{SIMIND} \left(\frac{Y_i}{Y_i^{SIMIND}} \right) \tag{4}$$

After scaling we smoothed the scatter sinogram using a (3 pixel FWHM) 3-D Gaussian filter to reduce noise effects.

We also investigated the global fraction model $s_i = \beta s_i^{SIMIND}$ where β can be obtained easily by calculating $\sum_i Y_i / \sum_i Y_i^{SIMIND}$. However, this model did not yield good reconstruction results empirically in our simulation studies. One possible explanation for this is that the SIMIND values $Y_i^{SIMIND}, s_i^{SIMIND}$ may be underestimated together or overestimated together locally. Therefore, the fraction α_i may be able to compensate for these estimation errors perhaps leading to a better scatter estimate s_i.

2.C. Phantom setup

2.C.1. Line source measurement to validate SIMIND

To validate SIMIND for ^{90}Y and our SPECT system, a line source measurement was performed. This measurement followed the NEMA guidelines for measuring (planar) spatial resolution, but the source geometry was adapted to provide a sufficient medium to generate bremsstrahlung photons. Instead of using a line source in 'air', a 1 mm diameter capillary tube filled with ^{90}Y in the form of a chloride solution (PerkinElmer) was positioned at the center of a small water filled vial 4.0-cm long and 1.5-cm in diameter (Fig. S1). The same phantom/camera geometry and gamma camera parameters used in the measurement (see section on Image Acquisition) were used for the SIMIND model.

2.C.2. Torso phantom measurement

A torso phantom with a fillable liver and lung compartments (Data Spectrum) was modified to include three intrahepatic 'lesions' (Fig. 2). The phantom compartments
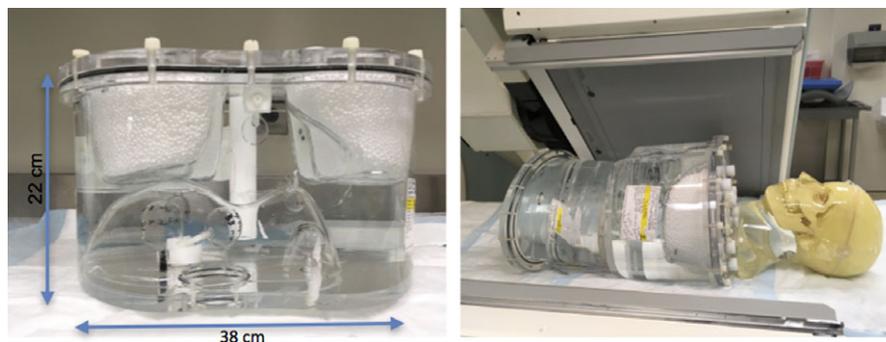

FIG. 2. The liver/lung torso phantom (left) was positioned in-between a skull and elliptical phantom for SPECT/CT imaging (right). [Color figure can be viewed at wileyonlinelibrary.com]

TABLE II. Activity concentrations used in the torso phantom experiment.

	Volume (mL)	Activity concentration MBq/mL[a]	Target-to-background activity concentration ratio
Normal liver (liver minus hepatic 'lesions')	1168	0.34	
Lung	2186	0.01	
Hepatic lesion 1 (sphere)	31	1.76	~5:1
Hepatic lesion 2 (sphere)	14	1.68	~5:1
Hepatic lesion 3 (ovoid)	28	1.63	~5:1
Extra-hepatic object 1 (sphere)	16	0.85	'Cold' background
Extra hepatic object 2 (sphere)	12	0.04	'Cold' background
Extra hepatic object 3 (ovoid)	10	0.2	'Cold' background

[a]Values need to be scaled by ×2.7 to get 'simulated' activity concentration since the phantom acquisition time was 2.7 times the typical acquisition time for patients.

(Table II) were filled with water mixed with a chelator to avoid adherence of ^{90}Y to the plastic walls.[25] ^{90}Y activities in the form of a chloride solution were carefully measured on a CRC-15 (Capintec) dose calibrator using the recommended dial setting #55 for ^{90}Y solutions in plastic syringes[26] and injected in to the compartments. The volume outside the liver and lungs was filled with 'cold' water. The activity concentrations and volumes of the various phantom compartments are given in Table II. These activity concentrations result in a lesion-to-normal liver activity concentration ratio of ~5:1 and a lung shunt of ~5% and were selected to mimic ratios typical for RE.[27–30] In addition, to assess visibility, three extrahepatic objects filled with very low activity concentrations (Table II) were positioned in the cold background to mimic inadvertent extra-hepatic deposition of microspheres. The total activity in the phantom was 566 MBq. To mimic events that are detected following scattering by tissue that is outside the camera field-of-view (FOV), a skull phantom and a uniform elliptical phantom both filled with 'cold' water was placed on either side of the liver/lung phantom (Fig. 2).

The liver concentration of 0.34 MBq/mL used in the phantom was limited by radiation safety requirements of the regulatory authority at our institution. Therefore, to mimic counting statistics typical in patient imaging the acquisition time was prolonged by a factor of 2.7 (80 sec/view for the phantom compared to 30 sec/view used in patients). The prolonged acquisition represents a 'simulated' liver activity concentration of 2.7 × 0.34 = 0.92 MBq/mL, which is clinically realistic for patient imaging following RE with glass microspheres (see for example the patient results discussed later).

2.D. Image acquisition and quantification

Images were acquired on a Siemens Symbia T6 SPECT/CT equipped with a high energy general purpose collimator

(hole length 59.7 mm, hole diameter 4 mm, septa 2 mm). A 105–195-keV bremsstrahlung acquisition window was selected (for all acquisitions in this paper) based on a preliminary simulation study investigating the primary-to-scatter ratio.[31] This range was also used in a previous study by Minarik et al.,[4] as it avoids characteristic x-rays (below ~80-keV) produced in the lead collimator and because the primary-to-scatter ratio decreases at > 200-keV.

For the planar measurement with the line source, the source was positioned 10-cm from the collimator and imaged with a 512 × 512 matrix (pixel size 1.2-mm). A background image for the same conditions was also acquired and subtracted from the line source image. SPECT/CT was acquired on the Siemens Symbia with the following acquisition parameters: 180° and 64 views per head with 80 sec/view (phantom) and 30 sec/view (patients); body contouring; step-and-shoot (phantom) or continuous motion (patients); and a 128 × 128 matrix with a pixel size of 4.8-mm. The CT component of acquisition used full circle rotation, 130-kV, 80-mAs and was reconstructed with a 512 × 512 × 196 matrix (0.98-mm × 0.98-mm × 2-mm voxel size). The CT-based attenuation map (at 150-keV) generated with the camera software was saved and used in our reconstruction.

To quantify activity in the phantom compartments, a calibration factor (CF) was computed for each reconstruction method by dividing the liver volume-of-interest (VOI) counts by the 'known' total liver activity. To convert counts to activity the SPECT voxel counts were multiplied by this CF. The liver relative calibration approach used here and in past dosimetry studies[29,32–35] is considered to be suitable for RE because the infused microspheres become permanently trapped in the micro capillaries of the treated liver and do not redistribute.

2.E. Phantom evaluation

We compared SPECT reconstruction, with and without scatter correction, using metrics for quantification accuracy, contrast, image noise, and visibility. For all of these metrics VOIs corresponding to the 'true' anatomical boundaries were defined on CT and applied to coregistered SPECT. The 'normal liver' is defined as the liver VOI minus the VOIs corresponding to the three intrahepatic lesions.

Quantification for object i is evaluated by comparing the SPECT estimated activity, A_i, with the true activity, A_i^{True}:

$$Activity\,Recovery = 100\% * A_i/A_i^{True} \qquad (5)$$

Contrast recovery for the hepatic lesions is calculated by:

$$CR_i = 100 * \frac{C_i/C_{BKG} - 1}{R - 1} \qquad (6)$$

where C_i is the mean counts for object I, C_{BKG} is the mean background (normal liver) counts and R is the true lesion-to-normal liver activity concentration ratio.

Noise in the background region is calculated as:

$$noise_{BKG} = 100\% \frac{STD_{BKG}}{C_{BKG}} \qquad (7)$$

where STD_{BKG} is the standard deviation of voxel counts in the background region. Here, background is defined as the normal liver eroded by 1-cm to avoid edge effects and spill-out from the lesions.

The contrast-to-noise ratio for the intrahepatic lesions and extrahepatic objects is calculated as:

$$CNR_i = (C_i - C_{BKG})/STD_{BKG} \qquad (8)$$

where, for the intrahepatic lesions, the background VOI is the normal liver while for the extra hepatic objects the background VOI is defined by a sphere of equal volume positioned in the 'cold' background in the vicinity of the object.

The ability of a human observer to detect low levels of ^{90}Y concentration was assessed based on the Rose criterion,[36] applied in the past to ^{90}Y PET imaging evaluations.[37,38] The visibility is related to both the CNR and the size of the object and is assessed by the detectability index:

$$V_i = CNR_i * \sqrt{N_i} \qquad (9)$$

where N_i is the number of voxels in the center slice of the object i.

2.F. Patient studies

2.F.1. Imaging and quantification

The SPECT reconstruction with MC scatter correction was evaluated in five patients treated with ^{90}Y RE at the University of Michigan Medical Center for cancer involving the liver. The routine treatment protocol for RE with glass microspheres (Theraspheres) was followed. The administered activity for the five patients ranged from 0.7 to 3.9 GBq while the lung shunt fraction ranged from 3% to 6%. Approval by the University of Michigan Internal Review Board (IRB) was obtained to access relevant patient information and imaging data to evaluate the current in-house developed reconstruction method. Post-therapy ^{90}Y SPECT acquisition time was 32 min and was performed within 1–3 hours post RE (prior to discharge) as part of the clinical protocol. The camera and other acquisition parameters for SPECT/CT were as described in the phantom study. In the 5 patients a trained Radiologist (RK) contoured a total of 11 well-defined hepatic lesions and the treated liver segment/lobe on baseline CT or MRI. Following coregistration contours were applied to ^{90}Y SPECT/CT images. As in the phantom study, the lesion and normal liver activities were quantified using the (liver) relative calibration factor computed individually for each patient and each reconstruction method. Here, the 'true' liver activity was set equal to the infused ^{90}Y activity corrected for the lung shunt fraction obtained from planar Tc-MAA imaging.

2.F.2. Statistical analysis

The lesion and normal liver activity concentrations and the lesion-to-normal liver uptake ratios without and with scatter correction were compared. For the lesion level outcomes (activity concentrations for individual lesions), the within-lesion

differences in outcome were analyzed in mixed effect models with a fixed effect for the mean difference between the two reconstruction methods. Patient level random intercepts were included to account for possible between-lesion, within-patient correlation. For the patient level outcomes (activity concentration in normal liver), a Wilcoxon signed rank test was used to test for any differences between the two reconstruction methods. Two-sided *P*-values less than 0.05 were considered significant and all analyses were performed in SAS 9.4.

3. RESULTS

3.A. Comparison of simulation with measurement

Figure 3 compares the simulated and measured line profiles that show excellent agreement. The FWHM and FWTM of the measured profile was 13.6 and 23.4-mm, respectively, while that of the simulated profile was 13.7 and 24.8-mm respectively. In addition, a SIMIND simulation corresponding to the experimental phantom setup was also performed and projections were compared with the measured projections. The profiles across the center of one of the projections are compared in Fig. 4 and show a high level of agreement in the distribution with some underestimation in the simulated counts. Note that in the projection images the low intensity 'line' below the liver corresponds to the air gap that was present between the liver phantom and the adjacent 'cold' elliptical phantom (Fig. 2), as they could not be placed directly next to one another due to the design of the phantoms. The contribution from scatter events in the 'cold' elliptical phantom is evident in the projection images.

3.B. Phantom reconstructions

3.B.1. Activity recovery, contrast recovery, and noise

The lesion contrast-to-noise ratio (averaged over the 3 liver lesions) and activity recovery for all VOIs are plotted
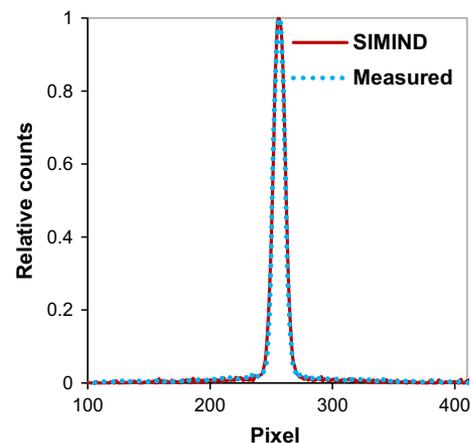

FIG. 3. Profile (10-pixel wide) across the measured and simulated line source. Profiles have been normalized to their maximum value. [Color figure can be viewed at wileyonlinelibrary.com]
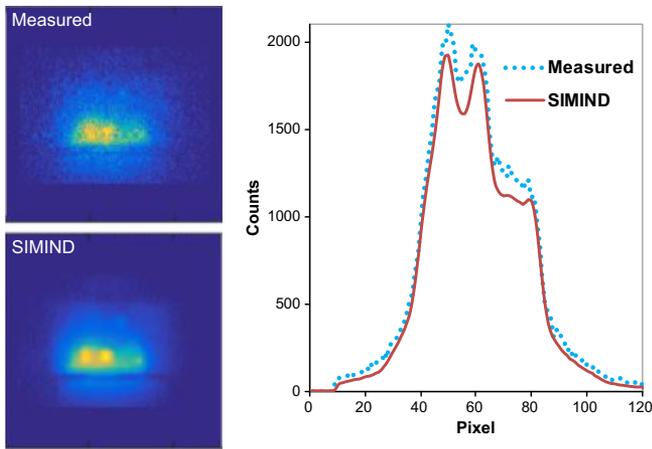
FIG. 4. Measured and simulated projection images (at 0^0) of the liver phantom and corresponding line profiles. Profiles were summed over 10 bins centered on the center sphere. [Color figure can be viewed at wileyonlinelibrary.com]

versus iteration and as a function of scatter update in Fig. 5 (all reconstructions used 8 subsets). These curves were the basis for selecting the number of scatter updates, the number of OS-EM iterations per update, and the total number of iterations for the results discussed in the rest of the paper. Without scatter correction, the CNR reaches a maximum at around five iterations, and therefore the first MC scatter estimate, MCS1, was obtained at this point. Similarly, based on the trends of the CNR plots, further scatter updates were made at 10 (MCS2) and 15 (MCS3) iterations. Since the CNR and activity recovery does not change substantially after two scatter updates, the results presented in the rest of the paper are with MCS1 and MCS2 only. Based on the convergence in activity recovery the total number of iterations was set to 15 iterations (eight subsets).

The profiles of Fig. S2 show the pixel-level scatter fractions $[s_i^{SIMIND}/Y_i^{SIMIND}$ of Eq. (4)] for the same projection as in Fig. 4. The scatter fractions ranged from around 0.6 to 0.8 for pixels corresponding to the liver region to 1.0 for pixels corresponding to cold regions. As evident in the figure there is good agreement between the true and estimated scatter fractions after just two MC updates. In the cold regions outside the liver and outside the phantom the scatter fraction is consistently underestimated (0.8–0.9 compared with the true value of 1.0).
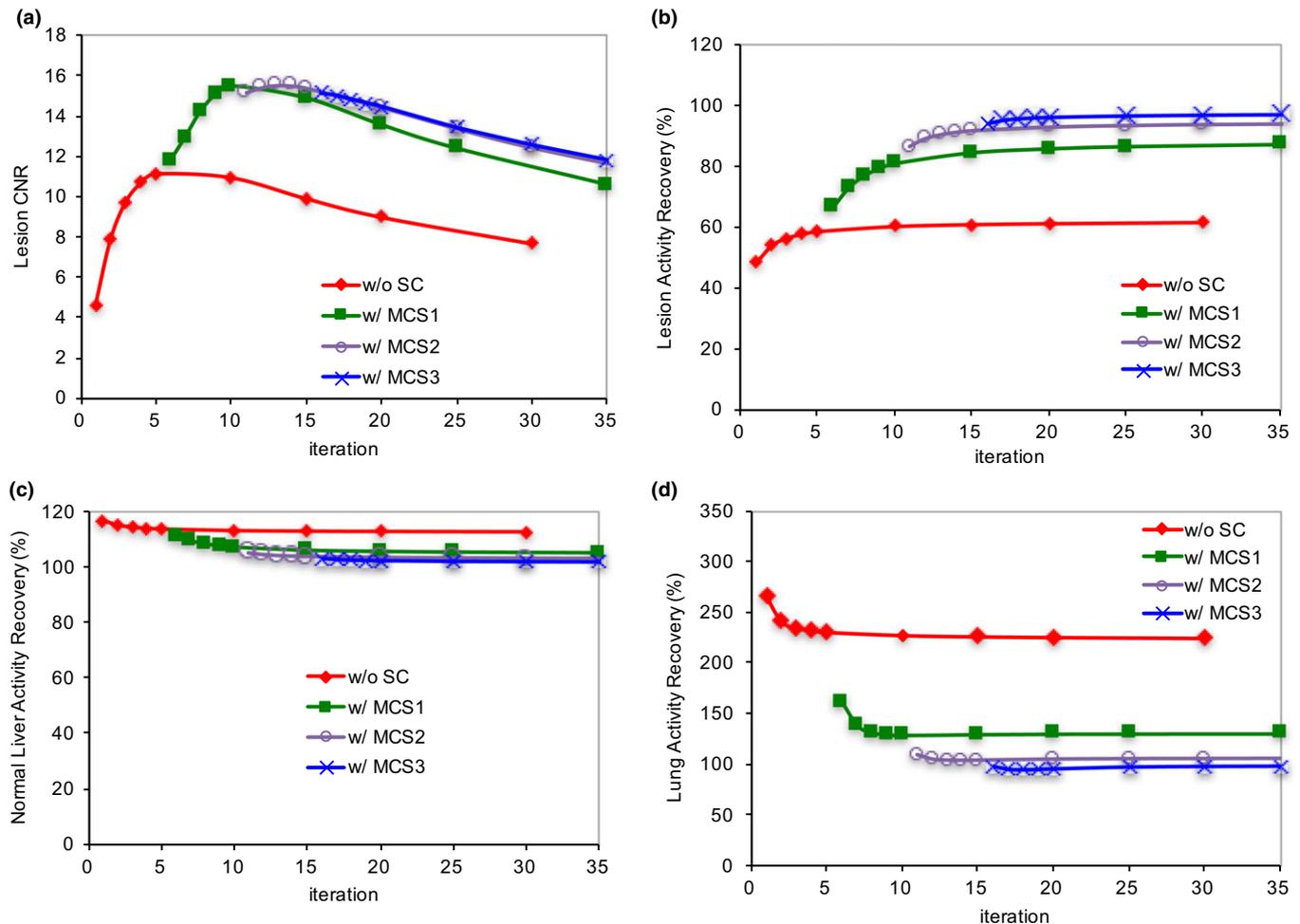

FIG. 5. (a) Lesion CNR, (b) lesion activity recovery, (c) normal liver activity recovery and (d) lung activity recovery for the different reconstructions of the phantom data. [Color figure can be viewed at wileyonlinelibrary.com]
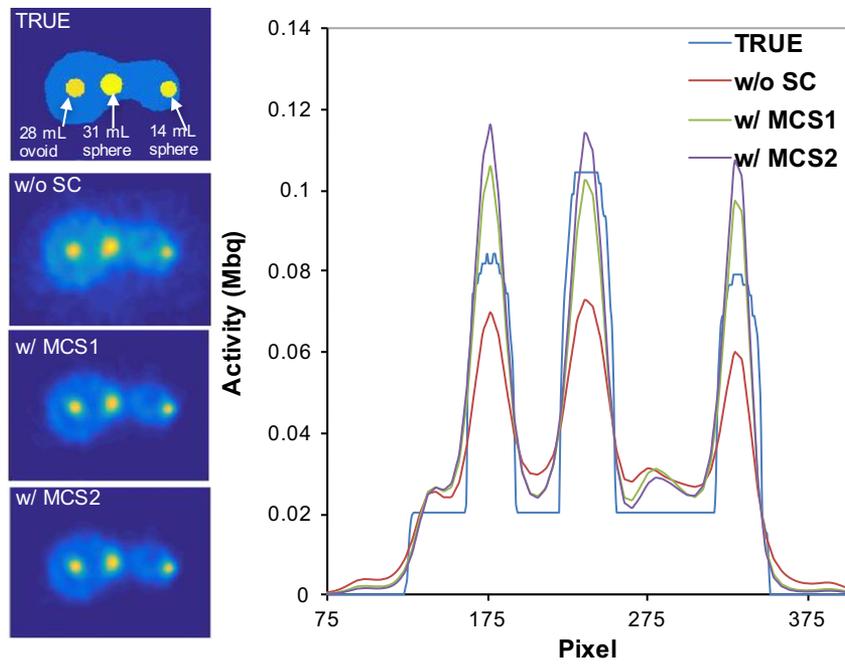
FIG. 6. An axial slice of the true activity map and the different reconstructions w/o and with SC and the corresponding line profiles for this slice. Profiles were summed over 30 bins centered on the center sphere. [Color figure can be viewed at wileyonlinelibrary.com]

Figure 6 shows a clear improvement in contrast between liver lesions and the normal liver as well as between the liver and the cold background when the MC scatter estimate is included in the reconstruction. Table III shows the quantitative improvement with scatter correction. Without scatter correction the normal liver activity is overestimated and the lesion activity is underestimated. Scatter correction substantially improves activity and contrast recovery in all volumes with only a small increase in noise. For lesions, activity recovery improved from > 55% without scatter correction to > 81% with a single MC scatter update and to > 86% after two updates. In lungs, reconstruction without scatter correction leads to a large overestimation of activity (recovery 227%) and two scatter updates are needed to achieve accurate activity recovery.

3.B.2. Visibility

Figure 7 demonstrates the qualitative improvement in detectability with scatter correction. The visibility index is very high for all objects except for the two extrahepatic objects with the lowest activity concentration when no scatter

correction is used (Table IV). However, with MC scatter correction the visibility for these two objects increased substantially (from 11 to 81 and from 8 to 27).

3.C. Patient studies

The reconstruction parameters selected based on the phantom CNR curves were also used in the patient study (15 total iterations with eight subsets, two scatter updates at iteration 5 and 10). Qualitatively, the increase in contrast with scatter correction is evident in the patient images (Figs. 8 and S3). This is especially true in the case of Fig. 8, which shows a large necrotic lesion with an enhancing rim. In Fig. 8, in addition to comparing the SPECT images comparison is also made to ^{90}Y PET, which was obtained with University of Michigan IRB approval for the purposes of research. The PET/CT data were acquired with a Siemens mCT scanner and was reconstructed with Siemens 3D-OS-EM software including point-spread function and time-of-flight information using 1 iteration, 21 subsets, and a 5-mm FWHM Gaussian postfilter. The matrix size was 200 × 200 (pixel size 4.07-mm). These PET parameters were chosen based on a

TABLE III. Activity recovery, contrast recovery and noise for the phantom experiment. All reconstructions used a total of 15 iterations (8 subsets).

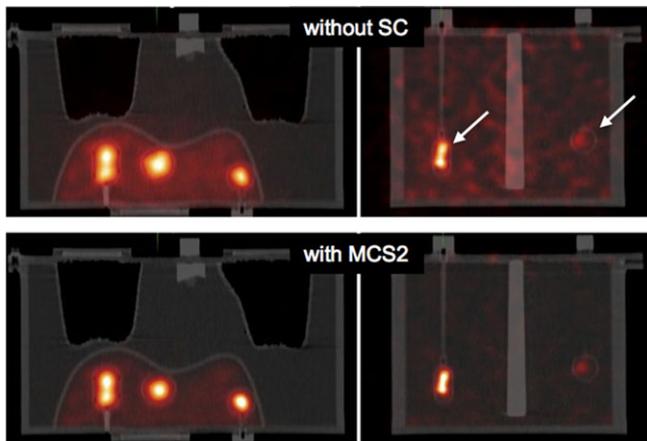|	Activity recovery (%)					Contrast recovery (%)			
	Normal liver	Lung	31 mL sphere	28 mL ovoid	14 mL sphere	31 mL sphere	28 mL ovoid	14 mL sphere	Noise (%)
w/o SC	113.0	226.5	62.6	65.2	54.6	44.5	46.2	34.7	13.0
w/MCS1	105.9	130.1	81.1	91.0	81.4	70.8	82.0	70.8	15.0
w/MCS2	103.8	103.9	85.9	99.0	90.2	78.4	94.1	83.4	16.5

FIG. 7. Coronal SPECT/CT slices without (top row) and with (bottom row) scatter correction, demonstrating visibility of the hepatic lesions (left) and the extra hepatic objects (right). [Color figure can be viewed at wileyonlinelibrary.com]

TABLE IV. Visibility for the hepatic lesions in 'warm' background and extra hepatic objects in 'cold' background.

		Visibility		
	Volume (mL)	w/o SC	w/MCS1	w/MCS2
Intrahepatic	31 mL sphere	79.3	105.4	105.3
Intrahepatic	28 mL ovoid	57.4	86.0	89.2
Intrahepatic	14 mL sphere	43.8	76.6	81.8
Extrahepatic	16 mL sphere	166.4	520.7	671.7
Extrahepatic	10 mL ovoid	11.1	58.2	81.0
Extrahepatic	12 mL sphere	8.0	22.3	26.5

previous phantom study.[39] The images and profiles of Fig. 8 show better contrast and agreement with PET when MC scatter estimation is included in the SPECT reconstruction. Without scatter correction the sharp drop in counts in the center (necrotic) part of the lesion is much less pronounced.

Table V compares lesion and normal liver activity concentration for the five patients estimated using the liver relative calibration from SPECT reconstructions without and with MC scatter estimation. For the 11 lesions, mean activity concentration is 4.9 (range 1.4 to 8.8) MBq/mL without scatter correction and 7.1 (range 1.4 to 12.7) MBq/mL with scatter correction ($P = 0.0547$). The mean normal liver activity concentration is 1.6 (range 1.1–2.2) MBq/mL without scatter correction and 1.5 (range 1.1–1.9) MBq/mL with scatter correction ($P = 0.056$). The mean lesion-to-liver uptake ratio is 2.7 (range 0.8 to 4.3) without scatter correction and 4.3 (range 1.0 to 9.1) with scatter correction (this difference was statistically significant with $P = 0.0402$). The same trends shown in Table III for the phantom study are demonstrated here for the patients: without scatter correction lesion activities are underestimated while the normal liver activity is overestimated when compared with scatter corrected SPECT. The only exceptions are the two large necrotic tumors in the liver of patient #3. In this case, the anatomical lesions outlined on

the CT are likely not a good representation of the viable lesions, and for this patient's lesions the outlines were therefore also defined by thresholding the SPECT, guided by the CT outline. With these functional lesion outlines, the activity concentrations estimated by SPECT without scatter correction were lower than those estimated with scatter correction (3.7 vs. 4.4 MBq/mL for lesion 1 and 3.2 vs. 3.7 MBq/mL for lesion 2).

3.D. Photon histories and simulation times

The MC scatter estimates for the phantom and patient studies discussed above were generated with 500 million photon histories per projection with a total simulation time of approximately 8 hours on a 12-core (2.7 GHz) Mac-pro personal computer. The effect of using fewer photon histories was investigated to determine the potential for reducing the simulation time. Reconstructions of the data for the phantom and for patient #3 were repeated with the scatter estimates generated using 50 and 5 million photons per projection, corresponding to simulation times of around 40 and 4 min respectively. Comparison of profiles across the reconstructed images show that results for 50 million photon histories are almost identical to those for 500 million photon histories, while visible differences are seen at 5 million histories (Fig. S4). The difference between total lesion counts for the 500 million history case is < 1.4% when histories are reduced to 50 million but up to 7.8% when histories are reduced to five million. Comparison of reconstructions corresponding to four realizations (with 4 different random seeds) of the 50 million case showed the difference between realizations to be < 0.8% for total lesion counts.

4. DISCUSSION

Model-based methods are necessary for scatter correction in 90Y SPECT because energy window-based methods are not feasible with the continuous bremsstrahlung energy spectrum. In the present study we implemented and validated a Monte Carlo based scatter estimation method, where the scatter estimate is combined with an analytical projector.

The high level of agreement between 90Y measurement and SIMIND shown here for our SPECT/CT system has been demonstrated before for other systems.[5] The slight underestimation in the tails of the line source profile (Fig. 3) is potentially due to photon scattering by the second camera head or surrounding objects not included in the camera model. In the phantom experiment there is further underestimation of counts (Fig. 4) because the phantom extended beyond the FOV, but the activity estimate and density map used as input to SIMIND are only available for the FOV as in patient imaging. Unlike a fully MC based reconstruction, our approach is not highly sensitive to small differences between measurement and simulation because MC is used only to generate the scatter fraction. The present phantom study mimicked the clinically realistic situation for RE where there is high uptake in the liver and low uptake in lungs surrounded by a cold
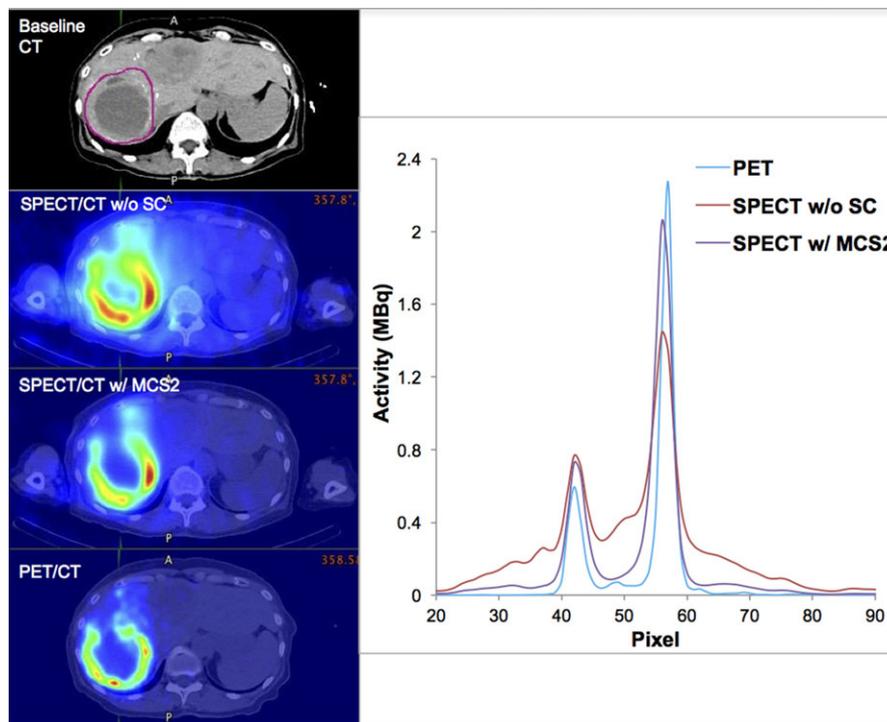
Fig. 8. For patient #3 the SPECT reconstruction without and with scatter correction is compared with ^{90}Y PET. Profiles are across the center of the large necrotic lesion contoured on the catheter directed selective hepatic arterial contrast enhanced CT. [Color figure can be viewed at wileyonlinelibrary.com]

TABLE V. Patient lesion and normal liver activity concentrations estimated from SPECT without and with scatter correction.

Patient #	Diagnosis		Volume (mL)	SPECT estimated concentration (MBq/mL)	
				w/o SC	With SC
1	Liver mets (NET[a])	Lesion 1	68.6	6.3	8.0
		Lesion 2	7.1	6.7	10.9
		Lesion 3	7.5	5.2	7.3
		Lesion 4	32.3	8.8	12.3
		Lesion 5	6.1	6.8	9.1
		Normal liver	1168	2.2	1.9
2	HCC[b]	Lesion 1	40.2	2.7	4.3
		Lesion 2	6.2	6.5	12.7
		Normal liver	1502	1.5	1.4
3	Liver mets (NET)	Lesion 1	820.3	1.6	1.6
		Lesion 2	523.4	1.4	1.4
		Normal liver	472	1.7	1.4
4	HCC	Lesion 1	27.3	3.7	4.3
		Normal liver	388	1.7	1.6
5	Liver mets (NET)	Lesion 1	17.2	4.2	6.1
		Normal liver	717.8	1.1	1.1

[a]NET, neuroendocrine tumor.
[b]HCC, hepatocellular carcinoma.

background. This is a more challenging condition in terms of scatter than past ^{90}Y imaging evaluations that have typically relied on geometries consisting of hot spheres in a uniform background.[6,8,37,38]

Our interest is in accurate quantification of lesion and normal liver activity for estimating mean absorbed dose as well as 3-D activity distributions for radiobiological dosimetry,[40] where low noise is of importance. Here, we show significant improvement in contrast recovery and activity recovery with MC scatter estimation with only a small degradation in noise (13% to 17% in Table III). Without scatter correction there is poor contrast, which translates to a significant underestimation of intrahepatic lesion activity and overestimation of the normal liver activity. For the normal liver, the overestimation in activity recovery went from 113% without scatter correction to 106% with a single update and 104% with two updates. For the smallest liver lesion, activity recovery improved from 55% without scatter correction to 81% with a single update of the scatter estimate and 90% with two updates. The lesion activity recoveries of the present study are somewhat higher than expected for SPECT imaging with a high-energy collimator, even with CDR modeling. This is attributed to the liver relative calibration used to quantify lesion activities and to imperfect scatter correction. If scatter is underestimated in the lesions relative to the liver some of the count loss due to partial volume effects is 'compensated' by uncorrected scatter counts.

Although lung-shunt calculations are performed prethrerapy with a Tc-MAA planning study, here we also investigated the accuracy in estimating the lung activity with ^{90}Y SPECT/CT, as this enables post-therapy verification of the delivered dose to the lung to evaluate potential toxicity. For the lung region where activity concentration is low, scatter is a much higher component of the total counts than in the liver, and

scatter modeling is even more challenging. In the present study, activity overestimation in the lung was as high as 226% without scatter correction and two updates of the scatter estimate were needed to achieve accurate activity recovery. The substantial improvement in the visibility index with scatter correction (Table IV) is particularly significant in the case of the extrahepatic objects in cold background due to safety concerns associated with unexpected microsphere deposition outside the liver. According to the Rose criteria an object is discernible when the visibility index is > 5[36]; however, as discussed in recent studies[37,38] this threshold depends on the size and shape of the lesion. When assessing 90Y PET acquisition protocols Carlier et al.[38] used a limit of > 8 for objects that are approximately circular in shape. In the present study, without scatter correction the visibility index was below this cutoff for the object with the lowest activity concentration, but well-exceeded this limit with scatter correction.

Our patient images and results re-enforces the trends observed with the phantom data. Without scatter correction patient lesion activity concentrations and the lesion-to-liver uptake ratios are substantially underestimated and liver activity concentration overestimated when compared to scatter corrected SPECT (Table V). These differences will translate to similar differences in absorbed dose estimation. With just 1–2 updates of the scatter estimate there was visible increase in contrast in the liver lesions (Figs. 8 and S3). For one patient with large necrotic lesions the SPECT images were compared with 90Y PET and the reconstruction with scatter correction showed better agreement with PET, which can be considered as the gold standard here. Given the lack of uptake in the center of the tumor accurate imaging can potentially determine which tumors may require boosts with external radiation therapies such as SBRT. The activity concentrations and lesion-to-liver uptake ratios of the present patient study can be compared with limited previous studies where these values were reported for RE with glass microspheres. Based on pretherapy Tc-MAA imaging Garin et al. reported[29] lesion-to-liver ratios of 0.6 to 25.9 (mean 7.2) for patients with HCC. Based on post-therapy 90Y SPECT using standard reconstruction without scatter correction, Kokabi et al. reported[32] lesion concentrations of 0.7–7.4 MBq/mL (mean 2.9) for patients with HCC.

Although our MC scatter estimate was used in a single-window acquisition/reconstruction approach here, it can be extended to a multiwindow approach, which will be the focus of a future study. The single window approach simplifies the reconstruction process as it allows the use of an attenuation map and CDR determined at a single energy. For this single-energy we used the center energy of the window while others[41] have used the mean energy of the window as it accounts for the energy dependence of the bremsstrahlung yield. However, that alternative would not significantly impact our results as the center energy and the mean energy in tissue are very close for the energy range considered here (150-keV vs. 142-keV). For the 105–195-keV range of the present study, the attenuation coefficient in tissue at the center energy is within 15% of the value at the lower and upper energy bounds of the window.[42] Phantom and patient results of the present study demonstrates that the count-rate with the relatively narrow window is sufficient for imaging following RE where there is high focal activity in the liver.

Limitations of the present study are that the phantom study evaluated relatively large (> 14 mL) lesions only and a single lesion-to-liver activity concentration ratio of 5:1. Although these values are typical for RE, there is a large range in lesion size and uptake ratios and these are well worth investigating in a future study. In addition, the quantification approach of the present study was limited to the relative calibration approach based on the assumption that the activity in the liver is known.[29,32–35] This has the advantage that a separate acquisition of a calibration phantom or source with known activity is not required to determine a CF that relates detected counts to activity. However, this approach is inadequate if the inadvertent deposition of microspheres outside the liver is significant or if the lung shut fraction is relatively large and substantially different from the pretherapy estimation. In a future study the relative calibration approach will be compared with that using an external CF, which should ideally be determined with a phantom geometry that approximates the patient, such as the liver/lung phantom of the present study. An advantage of a fully MC based reconstruction is that with a well-validated MC code quantitative results can be obtained without the need for a calibration measurement. However, our approach puts less demand on computational requirements than a fully MC approach. The present work demonstrated that accurate reconstruction can be achieved with just two scatter updates and with 50 million photon histories/per projection with a simulation time of around 40 min on a personal computer. Keeping the scatter component separate also facilitates combining our approach with commercial reconstruction software designed for conventional SPECT. It is feasible that the window-based scatter estimates typically available with commercial software can be replaced by a MC generated scatter estimate.

5. CONCLUSION

A 90Y bremsstrahlung SPECT reconstruction approach with MC based scatter estimation was implemented and evaluated. The relatively narrow single window used here for both the acquisition and projector modeling was shown to be sufficient for the RE application where there is high focal liver uptake, but may be inadequate for other applications with low count-rates. Phantom experiments showed substantial improvement in contrast and activity recovery without significant increase in noise with just two updates of the scatter estimate. Patient studies confirmed the trends observed in the phantom study with substantial underestimation of lesion activity concentration and lesion-to-liver uptake ratio without scatter correction compared with reconstruction with two updates of the MC scatter estimate. Evaluation of the required

number of photon histories showed that MC simulation time can be reduced by a factor of 10 without compromising results, which is promising for clinical implementation.

CONFLICT OF INTEREST

The authors declare that they have no conflict of interest.

a)Author to whom correspondence should be addressed. Electronic mail: yuni@umich.edu; Telephone: 734-647-2324.

REFERENCES

1. Kennedy A. Radioembolization of hepatic tumors. *J Gastrointest Oncol*. 2014;5:178–189.
2. Goldsmith SJ. Radioimmunotherapy of lymphoma: Bexxar and Zevalin. *Semin Nucl Med*. 2010;40:122–135.
3. https://www.clinicaltrials.gov/ct2/results?term=90Y&Search=Search. Accessed January 28, 2017.
4. Minarik D, Sjögreen Gleisner K, Ljungberg M. Evaluation of quantitative (90)Y SPECT based on experimental phantom studies. *Phys Med Biol*. 2008;53:5689–5703.
5. Rong X, Du Y, Ljungberg M, Rault E, Vandenberghe S, Frey EC. Development and evaluation of an improved quantitative 90Y bremsstrahlung SPECT method. *Med Phys*. 2012;39:2346–2358.
6. Elschot M, Lam MG, van den Bosch MA, Viergever MA, de Jong HW. Quantitative Monte Carlo based 90Y SPECT reconstruction. *J Nucl Med*. 2013;54:1557–1563.
7. Pasciak AS, Bourgeois AC, McKinne JM, et al. Radioembolization and the dynamic role of 90Y PET/CT. *Front Oncol*. 2014;4:38.
8. Willowson KP, Tapner M; QUEST Investigator Team, Bailey DL. A multicentre comparison of quantitative (90)Y PET/CT for dosimetric purposes after radioembolization with resin microspheres: the QUEST Phantom Study. *Eur J Nucl Med Mol Imaging*. 2015;42:1202–1222.
9. D'Arienzo M. Emission of β^+ particles via internal pair production in the $0^+ – 0^+$ transition of ^{90}Zr: historical background and current applications in nuclear medicine imaging. *Atoms*. 2013;1:2–12.
10. Smits ML, Elschot M, Sze DY, et al. Radioembolization dosimetry: the road ahead. *Cardiovasc Intervent Radiol*. 2015;38:261–269.
11. Uribe CF, Esquinas PL, Piwowarska-Bilska H, et al. Characteristics of bremsstrahlung emissions from radionuclide therapy isotopes. Proc. IEEE Nuc Sci Symp Med Imag Conf; 2013.
12. Simpkin DJ, Cullom SJ, Mackie T. The spatial and energy dependence of bremsstrahlung production about beta point sources in H_2O. *Med Phys*. 1992;19:105–114.
13. Bowsher JE, Floyd CE Jr. Treatment of compton scattering in maximum-likelihood, expectation-maximization reconstructions of SPECT images. *J Nucl Med*. 1991;32:1285–1291.
14. Daube-Witherspoon ME, Carson RE, Yen YC, Yap TK. Scatter correction in maximum-likelihood reconstruction of PET data IEEE Nucler Science Symposium and Medical Imaging Conference; 1992. Conference Record https://doi.org/10.1109/nssmic.1992.301098.
15. Dewaraja YK, Ljungberg M, Fessler JA. 3-D Monte Carlo-based scatter compensation in quantitative I-131 SPECT reconstruction. *IEEE Trans Nucl Sci*. 2006;53:181–188.
16. Moore SC, Ouyang J, Park MA, Fakhri GE. Monte Carlo-based compensation for patient scatter, detector scatter, and crosstalk contamination in In-111 SPECT imaging. *Nucl Instrum Methods Phys Res, Sect A*. 2006;569:472–476.
17. Zeng GL, Gullberg GT. Unmatched projector/backprojector pairs in an iterative reconstruction algorithm. *IEEE Trans Med Imaging*. 2002;19:548–555.
18. Nguyen MP, Kim H, Chun SY, Fessler JA, Dewaraja YK. Joint spectral image reconstruction for 90Y SPECT with multi-window acquisition. Proc. IEEE Nuc Sci Symp Med Imag Conf; 2015.
19. Zeng GL, Gulbert GT. Frequency domain implementation of the three-dimensional geometric point response correction in SPECT imaging. *IEEE Trans Nucl Sci*. 1992;39:1444–1453.
20. Ljungberg M. The SIMIND Monte Carlo program. In: Ljungberg M, Strand SE, King MA, eds. *Monte Carlo Calculation in Nuclear Medicine: Application in Diagnostic Imaging*, 2nd edn. Florida: Taylor & Francis; 2012.
21. Rault E, Staelens S, Van Holen R, De Beenhouwer J, Vandenberghe S. Fast simulation of yttrium-90 bremsstrahlung photons with GATE. *Med Phys*. 2010;37:2943–2950.
22. Dewaraja YK, Ljungberg M, Koral KF. Characterization of scatter and penetration using Monte Carlo simulation in 131I imaging. *J Nucl Med*. 2000;41:123–130.
23. Chun SY, Fessler JA, Dewaraja YK. Correction for collimator-detector response in SPECT using point spread function template. *IEEE Trans Med Imaging*. 2013;32:295–305.
24. Koral KF, Yendiki A, Dewaraja YK. Recovery of total I-131 activity within focal volumes using SPECT and 3D OSEM. *Phys Med Biol*. 2007;52:777–790.
25. Park M-A, Mahmood A, Zimmerman RE, Limpa-Amara N, Makrigiorgos GM, Moore SC. Adsorption of metallic radionuclides on plastic phantom walls. *Med Phys*. 2008;35:1606–1610.
26. Zimmerman B, Cessna J, Millican M. Experimental determination of calibration settings for plastic syringes containing solutions of 90Y using commercial radionuclide calibrators. *Appl Radiat Isot*. 2004;60:511–517.
27. Campbell JM, Wong CO, Muzik O, Marples B, Joiner M, Burmeister J. Early dose response to yttrium-90 microsphere treatment of metastatic liver cancer by a patient-specific method using single photon emission computed tomography and positron emission tomography. *Int J Radiat Oncol Biol Phys*. 2009;74:313–320.
28. Kao YH, Hock Tan AE, Burgmans MC, et al. Image-guided personalized predictive dosimetry by artery-specific SPECT/CT partition modeling for safe and effective 90Y radioembolization. *J Nucl Med*. 2012;53:559–566.
29. Garin E, Lenoir L, Rolland Y, et al. Dosimetry based on 99 mTc-macroaggregated albumin SPECT/CT accurately predicts tumor response and survival in hepatocellular carcinoma patients treated with 90Y-loaded glass microspheres: preliminary results. *J Nucl Med*. 2012;53:255–263.
30. Kao YH, Magsombol BM, Toh Y, et al. Personalized predictive lung dosimetry by technetium-99 m macroaggregated albumin SPECT/CT for yttrium-90 radioembolization. *Eur J Nucl Med Mol Imaging Res*. 2014;4:33.
31. Dewaraja YK, Roberson P, Clinthorne N, et al. Quantitative bremsstrahlung SPECT/CT image reconstruction with patient specific Monte Carlo scatter compensation for 90Y microsphere radio embolization [abstract]. *J Nucl Med*. 2012;53:444.
32. Kokabi N, Galt JR, Xing M, et al. A simple method for estimating dose delivered to hepatocellular carcinoma after yttrium-90 glass-based radioembolization therapy: preliminary results of a proof of concept study. *J Vasc Interv Radiol*. 2014;25:277–287.
33. Chiesa C, Mira M, Maccauro M, et al. Radioembolization of hepatocarcinoma with (90)Y glass microspheres: development of an individualized treatment planning strategy based on dosimetry and radiobiology. *Eur J Nucl Med Mol Imaging*. 2015;42:1718–1738.

34. Pacilio M, Ferrari M, Chiesa C, et al. Impact of SPECT corrections on 3D-dosimetry for liver transarterial radioembolization using the patient relative calibration methodology. *Med Phys*. 2016;43:4053–4064.

35. Strigari L, Sciuto R, Rea S, et al. Efficacy and toxicity related to treatment of hepatocellular carcinoma with 90Y-SIR spheres: radiobiologic considerations. *J Nucl Med*. 2010;51:1377–1385.

36. Cherry SR, Sorenson JA, Phelps ME. *Physics in Nuclear Medicine*, 4th edn. Philadelphia, PA: Elsevier; 2003.

37. Van Elmbt L, Vandenberghe S, Walrand S, Pauwels S, Jamar F. Comparison of yttrium-90 quantitative imaging by TOF and non-TOF PET in a phantom of liver selective internal radiotherapy. *Phys Med Biol*. 2011;56:6759–6777.

38. Carlier T, Eugène T, Bodet-Milin C, et al. Assessment of acquisition protocols for routine imaging of 90Y using PET/CT. *Eur J Nucl Med Mol Imaging Res*. 2013;3:11.

39. Dewaraja YK, Novelli PM, Fessler JA, et al. 90Y imaging for dosimetry in radioembolization: comparison between scatter corrected bremsstrahlung SPECT/CT and time-of-flight PET/CT [abstract]. *Eur J Nucl Med Mol Imaging*. 2015;42:S156.

40. Cremonesi M, Chiesa C, Strigari L, et al. Radioembolization of hepatic lesions from a radiobiology and dosimetric perspective. *Front Oncol*. 2014;4:210.

41. Siman W, Mikell JK, Kappadath SC. Practical reconstruction protocol for quantitative (90)Y bremsstrahlung SPECT/CT. *Med Phys*. 2016;43:5093–5103.

42. White DR, Griffith RV, Wilson IJ. *Photon, Electron, Proton and Neutron Interaction Data for Body Tissues*. ICRU Report 46. Bethesda, MD: International Commission on Radiation Units and Measurements; 1992.

SUPPORTING INFORMATION

Additional Supporting Information may be found online in the supporting information tab for this article.

Fig. S1. ^{90}Y line source positioned at the center of a 4.0 cm long 1.5 cm diameter water filled vial.

Fig. S2. Profiles across the 'true' and estimated scatter fractions ($s_i^{\text{SIMIND}}/Y_i^{\text{SIMIND}}$) for the same projection as in Fig. 4. The 'true' scatter fractions correspond to MC simulation of the true activity map, while the estimated scatter fractions correspond to MC simulation of the SPECT measured activity map. Profiles were summed over 10 bins centered on the center sphere. The phantom extends from pixel 25 to 105 and the liver from pixel 38 to 84.

Fig. S3. Axial slice of the baseline CT and SPECT/CT without and with scatter correction for patient #4. The lesion contour defined on baseline CT is applied to coregistered SPECT/CT.

Fig. S4. Profiles across the phantom image of Fig. 6 (left) and patient image of Fig. 8 (right) as a function of the number of photon histories (per projection) used to generate the MC scatter estimate.

Fig. S1. ^{90}Y line source positioned at the center of a 4.0 cm long 1.5 cm diameter water filled vial.

Fig. S2. Profiles across the 'true' and estimated scatter fractions ($s_i^{SIMIND}/Y_i^{SIMIND}$) for the same projection as in Fig. 4. The 'true' scatter fractions correspond to MC simulation of the true activity map, while the estimated scatter fractions correspond to MC simulation of the SPECT measured activity map. Profiles were summed over 10 bins centered on the center sphere. The phantom extends from pixel 25 to 105 and the liver from pixel 38 to 84.

Fig. S3. Axial slice of the baseline CT and SPECT/CT without and with scatter correction for patient #4. The lesion contour defined on baseline CT is applied to co-registered SPECT/CT.

Fig. S4. Profiles across the phantom image of Fig. (left) and patient image of Fig. (right) as a function of the number of photon histories (per projection) used to generate the MC scatter estimate.
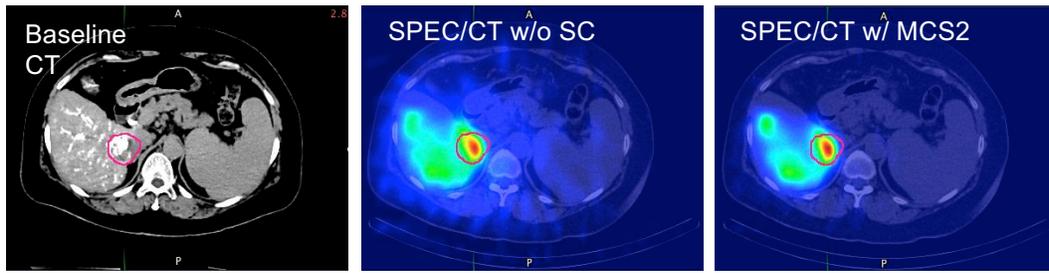
SUPPLEMENTARY FIG. 3. Axial slice of the baseline CT and SPECT/CT without and with scatter correction for patient #4. The lesion contour defined on baseline CT is applied to co-registered SPECT/CT.